A Nonlinear Ultrasonic Modulation Approach for the Detection and Localisation of Contact Defects

Christos Andreades, Gian Piero Malfense Fierro, Michele Meo
Department of Mechanical Engineering, University of Bath, Bath BA2 7AY, UK

Abstract

Critical metallic and composite structures are periodically inspected for contact defects such as kissing bonds and delamination, using phased array techniques based on linear ultrasound. The detection of contact flaws at multiple depths in the material can be challenging due to high signal attenuation and noise level. In this study an alternative ultrasonic phased array approach relying on the nonlinear modulation of dual-frequency excitation was introduced to improve the sensitivity and accuracy in the detection of contact defects. A phased array probe was used for the generation of single-frequency and dual-frequency waves, and the capturing of echoes. The flaws were detected using a new nonlinear modulated parameter characterising the response of the material arising only from the modulation sidebands at the sum and difference frequencies f_2+f_1 and f_2-f_1. Ultrasonic tests were conducted on materials with multiple contact interfaces. The novel parameter was plotted against the linear response, and the peaks indicating the contact interfaces were compared based on their signal-to-noise ratio (*SNR*), their width at half-height (6 dB drop) and their positioning error. The peaks of the nonlinear modulated parameter offered up to 10^3 times higher *SNR*, up to 10 times smaller width at half-height and around 45% smaller localisation error than the peaks in the classical linear ultrasonic response. The results showed that the proposed approach could lead to more effective detection and more accurate localisation of contact defects in structural materials such as kissing bonds and closed delamination.

Keywords: Contact Acoustic Nonlinearity, Nonlinear Ultrasound, Nonlinear Phased Array, Modulation, Contact Interface, Kissing Bond, Internal Defect.

1 Introduction

Contact type defects can be found in metallic and composite structures in the form of kissing bond, closed crack, delamination and debonding [1]. This defect type can be described as an interface of plastic contact between the surfaces of two elastic solid layers with similar material properties. The layers are typically separated by a gap due to surface imperfections/roughness, meaning that a contact interface has no strength [2]. For this reason, the early identification of such flaws has been a significant requirement in non-destructive evaluation (NDE) of materials.

Contact defects of certain size are detectable using various linear ultrasonic methods relying on the interaction of propagating waves with the contact interface [3-6]. This interaction causes reflections, scattering and attenuation of waves that can be recorded by the same ultrasonic source or other transducers. Among these, linear pulse-echo techniques using phased arrays of piezoelectric elements are widely preferred for the inspection of internal defects in many aerospace, automotive and civil structures [7-9]. They enable quick acquisition of multiple one-dimensional amplitude waveforms (A-scans) that can be added to provide a cross-sectional amplitude image (B-scan) of the inspected medium. In addition, the array elements can be excited in a specific order and according to pre-set delay laws to achieve steering or focusing of ultrasonic wave beams for improved localisation and sizing of damage [10, 11]. Various studies on linear phased array methods demonstrated effective identification of contact flaws at a single interface in metallic or composite parts [12-16], but only few of them detected multiple defect interfaces through the material thickness [17, 18]. This can be very challenging, depending on the mechanical contact between the surfaces at each damaged plane. In the case of multiple contact defects with almost perfectly mated surfaces, the propagating waves are transmitted through the interfaces, meaning that the amplitude of reflected waves will be relatively low [19]. For a given noise level in the signal, such reflections may not be detectable. Equally, in a poor-contact scenario most of the incident wave energy will be reflected to the source from the first interface, thus only low-amplitude waves will be reflected from any interfaces existing deeper in the material [20]. Hence, new ultrasonic methods of higher sensitivity to defect identification are required.

Over the last years, different research studies proposed nonlinear ultrasonic phased array techniques. In general, ultrasonic methods focusing on the assessment of acoustic nonlinearities in the material response have shown higher accuracy to the detection of micro-defects than linear ultrasonic methods, especially at the early stages of damage formation [21]. Briefly, under single-frequency (f_1) excitation, nonlinearities are detectable in the received signal spectrum in the form of higher harmonics ($2f_1, 3f_1$ etc.) and sub-harmonics ($f_1/2$, $f_1/3$ etc.) [22-24]. Based on that, some studies demonstrated accurate monitoring of fatigue crack growth in metallic samples using nonlinear phased array methods relying on the measurement of the second harmonic [25], the sub-harmonics [26-29] and the diffuse field energy [30, 31]. However, higher harmonic and sub-harmonic generation can be partially or totally related to system/instrumentation nonlinearities, and the acquisition of the diffused field of all array elements is time consuming and requires advanced signal

processing [31, 32]. Alternatively, recent studies focused on the development of nonlinear phased array methods based on ultrasonic wave modulation of signals with two frequencies. In fact, under dual-frequency (f_1 and f_2) excitation, modulation sidebands can be generated in the received spectrum at the sum and difference frequencies ($f_s = f_2 + f_1$ and $f_d = f_2 - f_1$) [33, 34]. The main advantage of wave modulation technique is that the amplitude of generated sidebands is less affected by equipment nonlinearities, compared with the amplitude of generated harmonics [1, 35-38]. Thus, the detection of spectral sidebands is more likely to be attributed to the presence of defects. In addition, it is relatively easier to satisfy the conditions necessary for defect excitation by using input waves of two different frequencies instead of a single frequency [38]. For example, Haupert et al. introduced an amplitude modulation method relying on image acquisition from phased arrays, where the linear material response is subtracted from the modulated signal revealing the image of nonlinear scattering in steel specimens with thermal fatigue cracks [39, 40]. Alston et al. focused on the detection of a kissing bond between two aluminium blocks based on non-collinear mixing of shear waves from two sources producing nonlinear longitudinal waves at sum-frequency that were captured by a phased array of sensors [41]. Finally, in a previous study of Fierro and Meo, a nonlinear frequency and amplitude modulation evaluation (FAME) technique was developed for more accurate detection of fatigue crack tips in aluminium specimens through phased array testing. This method focused on the assessment of acoustic nonlinearities based on the combined response of modulation sidebands and higher harmonics, after filtering out the linear ultrasonic effects [42].

Although the above nonlinear techniques offered improved sensitivity to micro-flaws compared with conventional linear ultrasonic methods, these were demonstrated on experimental samples containing a single interface of damage, and in most cases, the defects were oriented vertically relative to the plane of phased array elements. The identification of contact defects at multiple interfaces through the material remains challenging because the generation of detectable nonlinearities requires high amplitudes and signals of long duration, which is usually an equipment limitation for ordinary phased array systems [42].

This study introduces an optimised version of the phased array technique developed by Fierro and Meo [42], capable of identifying multiple contact interfaces in metallic and composite materials. In fact, this method focuses on the improvement of signal-to-noise ratio (*SNR*) relative to the case of linear ultrasonic testing, to enable more sensitive and accurate detection of peaks in the time domain of the received signal. The proposed version is also relying on the nonlinear modulation of ultrasonic waves from dual-frequency excitation. However, the acoustic nonlinearities generated by the damage were assessed using a parameter describing the nonlinear modulated response of the material arising only from the sidebands at f_s and f_d. This is achieved by employing the pulse inversion technique in some of the signal processing steps, to filter out both the fundamental and the second-order frequency harmonics from the captured signals [43, 44]. The performance of the presented method was compared with that of conventional linear ultrasonic inspection, by performing phased array (pulse-echo) experiments on aluminium and CFRP samples containing multiple horizontal interfaces of contact defects.

2 Elastic Wave Propagation Through Contact Interfaces

As illustrated in Figure 1, a contact defect can be considered the interface between the surfaces of two similar elastic solid layers, that are separated by a gap of height h due to material imperfections/roughness. According to Richardson [45] and Biwa et al. [46], the value of h is a function of the contact pressure p. In the absence of ultrasonic excitation, the layers are assumed to be at equilibrium under static pressure p_0 and the gap height is $h_0 = X_+ - X_-$ (i.e. $p(h_0) = p_0$).

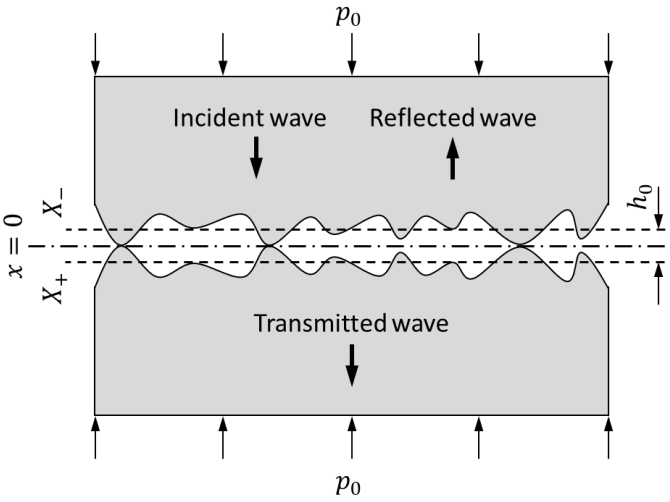

Figure 1: Longitudinal wave propagation through contact interface between two material layers held under pressure.

When longitudinal elastic waves are propagating perpendicularly to the plane of the interface, the equation of wave motion is

$$\rho \frac{\partial^2 u}{\partial t^2} = \frac{\partial \sigma}{\partial x} \tag{1}$$

where ρ is the material density, $u(x,t)$ is the wave displacement, t is the time, $\sigma(x,t) = E\varepsilon - p_0$ is the stress, E is the material elasticity (Young's modulus) and $\varepsilon = \frac{\partial u}{\partial x}$ is the strain. As the waves interact with contact surfaces, part of the incident wave energy is reflected to the source and part of it is transmitted through the interface (Figure 1). Based on this, the solution to equation (1) can be expressed as

$$u(x,t) = u_I(x - ct) + u_R(x + ct) \quad \text{for} \quad x < 0 \tag{2a}$$

and

$$u(x,t) = u_T(x - ct) \quad \text{for} \quad x > 0\,, \tag{2b}$$

where $c = \sqrt{E/\rho}$ is the longitudinal wave speed and u_I, u_R and u_T represent the displacement fields of the incident, reflected and transmitted waves [45, 46]. In addition, an amount of p is applied on the mated surfaces by the incident waves. This results in the variation of the h with time (opening-closing motion), in a nonlinear manner described by the following expression

$$h(t) = h_0 + u(X_+, t) - u(X_-, t). \tag{3}$$

Hence, the contact interface is subject to a continuous stress that relies on the relationship between p and h. By considering the case of dual-frequency excitation of the contact surfaces using two monochromatic sinusoidal waves with frequencies f_1 and f_2 and amplitudes A_1 and A_2, the incident wave can be written as

$$u_I(x-ct) = A_1 cos\left[\frac{2\pi f_1}{c}(x-ct)\right] + A_2 cos\left[\frac{2\pi f_2}{c}(x-ct)\right]. \quad (4)$$

The explicit analysis provided in the study of Guo et al. [47], which followed the works of Richardson [45] and Biwa et al. [46], showed that both the reflected and the transmitted signals would exhibit linear harmonics at f_1 and f_2 frequencies with A_{f_1} and A_{f_2} amplitudes, second-order nonlinear harmonics at $2f_1$ and $2f_2$ frequencies with A_{2f_1} and A_{2f_2} amplitudes, and first-order nonlinear intermodulation peaks (sidebands) at the sum-frequency ($f_s = f_2 + f_1$) and the difference-frequency ($f_d = f_2 - f_1$) with A_s and A_d amplitudes. The A_{2f_1} and A_{2f_2} were found to be proportional to the square of A_{f_1} and A_{f_2}, respectively, whereas A_s and A_d were linear functions of the product of A_{f_1} and A_{f_2}. Hence, the dependency of the interface nonlinearity to the contact pressure was successfully monitored by calculating the magnitude of the relative acoustic nonlinearity parameters β_s and β_d corresponding the spectral sidebands

$$\beta_s \approx \frac{A_s}{A_{f_1} A_{f_2}} \quad (5a)$$

and

$$\beta_d \approx \frac{A_d}{A_{f_1} A_{f_2}}. \quad (5b)$$

The technique used in this study relied on the detection of the acoustic nonlinearities using the nonlinear modulated response ($R_{\beta_s+\beta_d}$) of the material, which is calculated as the sum of β_s and β_d parameters

$$R_{\beta_s+\beta_d} = \beta_s + \beta_d \approx \frac{A_s + A_d}{A_{f_1} A_{f_2}}. \quad (6)$$

Before moving to the explanation of the technique and how $R_{\beta_s+\beta_d}$ can be practically obtained, it must be noticed that when the contact interface is excited using ultrasonic waves of single-frequency (e.g. f_1), the reflected and the transmitted signals contain the second-order nonlinear harmonic at $2f_1$ (and higher-order harmonics) without any intermodulation products. The studies of Biwa et al. [46] and Kim and Lee [2] showed that, in such case, the level of interface nonlinearity could be monitored using the following relative acoustic nonlinearity parameter

$$\beta \approx \frac{A_{2f_1}}{{A_{f_1}}^2} \quad (7)$$

However, as mentioned and referenced in the Introduction section, the main benefit of dual-frequency over single-frequency transmission is that the amplitude of modulation sidebands (A_s and A_d) is less influenced by the nonlinearities induced by the power instruments of the setup relative to the second harmonic amplitude (A_{2f_1}).

At this point, it is important to be mentioned that the theory provided in this section concerns the classical nonlinear effects generated by the dynamics of contact-type damage. In reality, there is a number of additional phenomena contributing to the nonlinear response of damaged materials such as the relative (frictional) movement of contact surfaces accompanied by temperature field generation, elastic hysteresis, local hardening, etc. In any case, the presented phased array technique should be equally effective in the identification of contact defects.

3 Phased Array Method based on Nonlinear Ultrasound Modulation

The nonlinear phased array method used in this study is an optimised version of the FAME method introduced by Fierro and Meo [42]. To obtain the $R_{\beta_s+\beta_d}$ response of the material under ultrasonic phased array inspection, the four signals illustrated in Figure 2 are required. The difference between those signals is the order in which the elements of the phased array probe are generating waves at f_1 and f_2 frequencies. For the first signal, waves are transmitted from all the elements at f_1 (i.e. signal u_{f_1}), whereas for the second one at f_2 (i.e. signal u_{f_2}). This allows the recording of the linear ultrasonic response of the samples at these two frequencies. For the third signal, waves are fired at f_1 from the odd-numbered elements and at f_2 from the even-numbered elements (i.e. signal $u_{f_{12}}$), to achieve nonlinear modulation of the propagating waves. The last signal has the inverse element order of the third one (i.e. signal $u_{f_{21}}$). It is worth noting that the sum of $u_{f_{12}}$ and $u_{f_{21}}$ results in the same amount of transmitted energy at f_1 and f_2 as with the individual u_{f_1} or u_{f_2}, because for $u_{f_{12}}$ and $u_{f_{21}}$ only half of the array elements are generating f_1 and f_2 waves.

In addition, the input signals are focused on the back surface of the samples because in a real case of inspection the depth of possible contact defects will be unknown. Moreover, for $u_{f_{12}}$ and $u_{f_{21}}$ signals, a delay is applied between the transmission of waves at f_1 and f_2 frequencies. Specifically, element firing at f_2 starts immediately after element firing at f_1 has stopped (i.e. delayed by a period of $1/f_1$). In this way, the waves propagating at f_1 can reach and excite the contact surfaces first, and then the waves travelling at f_2 will arrive and modulate this excitation.

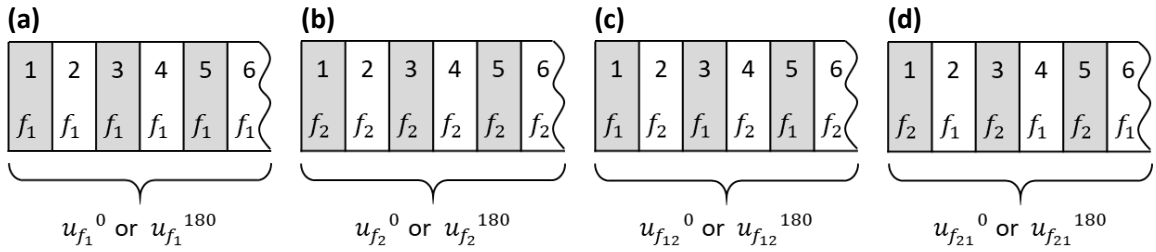

Figure 2: Frequency order of phased array elements in signal u_{f1} (a), signal u_{f2} (b), signal u_{f12} (b) and signal u_{f21} (d). The numerical superscripts indicate the 0° and 180° phase angles respectively.

The transmission of the above four signals is initially performed with a phase angle of 0° ($u_{f_1}{}^0$, $u_{f_2}{}^0$, $u_{f_{12}}{}^0$ and $u_{f_{21}}{}^0$), and then with a phase angle of 180° ($u_{f_1}{}^{180}$, $u_{f_2}{}^{180}$, $u_{f_{12}}{}^{180}$ and $u_{f_{21}}{}^{180}$). This is also known as pulse inversion, and it is a common method in literature for the cancellation of the fundamental harmonics at f_1 and f_2 [48-50]. The frequency spectrum resulting from the summation of the signals captured under single- or dual-frequency excitation with 0° and 180° phase angles is presented in Figure 3. Ideally, by adding the 0° and 180° signals, the fundamental harmonic amplitudes (A_{f_1} and A_{f_2}) will be minimised because the signals are identical in amplitude and wavelength, but opposite in phase. In the case of single-frequency excitation (Figure 3c and Figure 3d), the amplitude of second harmonics ($A_{2f_1}$and A_{2f_2}) after adding the 0° and 180° signals will be doubled since the nonlinear waves generated at the contact interfaces are propagating in phase. For dual-frequency signals (Figure 3e and Figure 3f), $A_{2f_1}$and A_{2f_2} will not be doubled because, as explained in the previous paragraph, the sum of harmonic amplitudes is equal to the individual harmonic amplitudes in u_{f_1} or u_{f_2} signals (i.e. same number of firing elements in total).

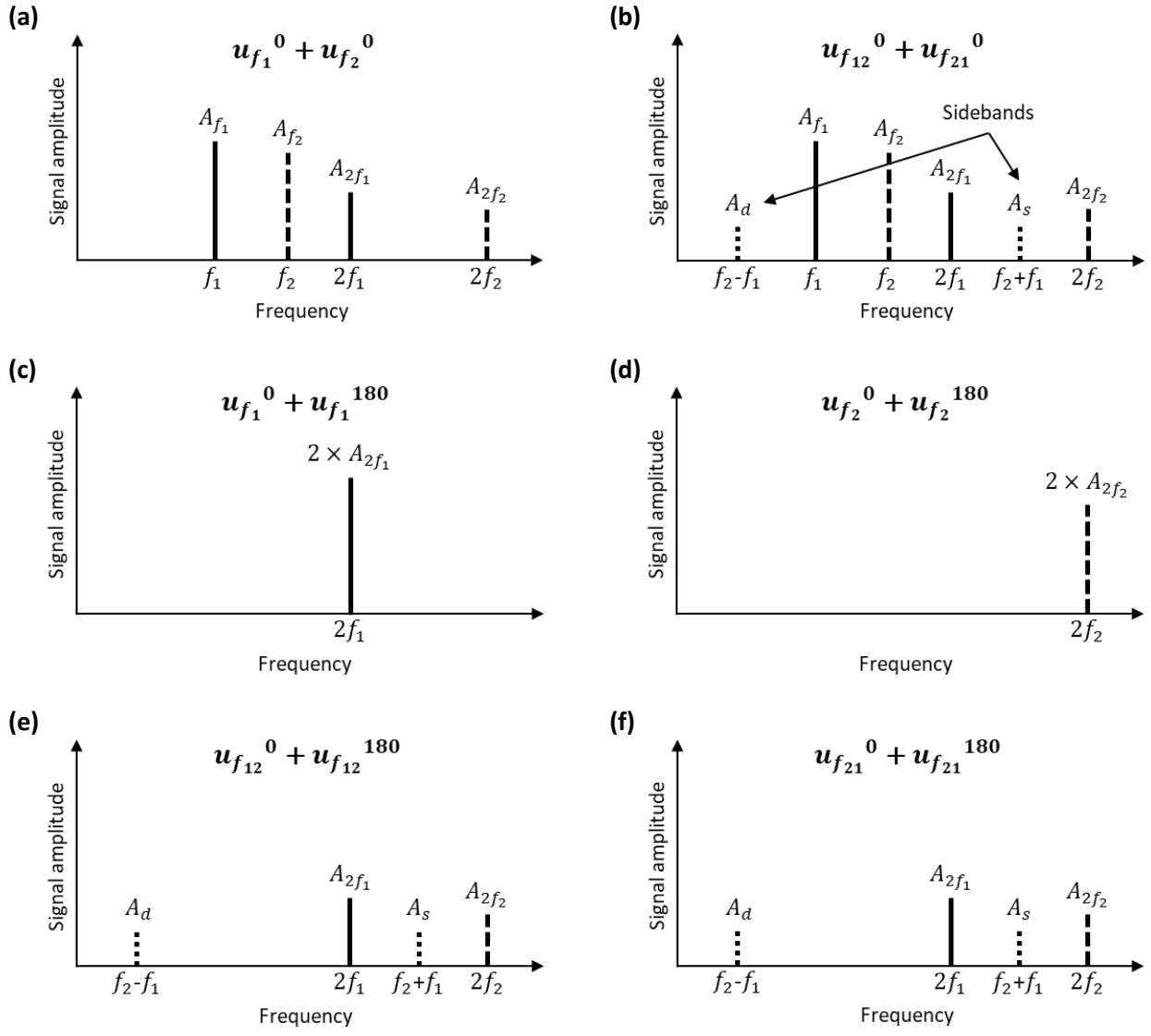

Figure 3: Illustration of the frequency spectrum resulting from signal summation $u_{f1}{}^0 + u_{f2}{}^0$ (a), $u_{f12}{}^0 + u_{f21}{}^0$ (b), $u_{f1}{}^0 + u_{f1}{}^{180}$ (c), $u_{f2}{}^0 + u_{f2}{}^{180}$ (d), $u_{f12}{}^0 + u_{f12}{}^{180}$ (e) and $u_{f21}{}^0 + u_{f21}{}^{180}$ (f).

Based on the above, the response corresponding to the sum of sideband components ($R_{sideband}$), and the response corresponding to the product of fundamental harmonics ($R_{fund.\ harm.}$) can be obtained by inserting the captured time signals in the following expressions

$$R_{sideband} = \left[\left({u_{f_1}}^0 + {u_{f_2}}^0\right) - \left({u_{f_1}}^0 \ + \ {u_{f_1}}^{180}\right) - \left({u_{f_2}}^0 \ + \ {u_{f_2}}^{180}\right)\right] \\ -\left[\left({u_{f_{12}}}^0 + {u_{f_{21}}}^0\right) - \left({u_{f_{12}}}^0 \ + \ {u_{f_{12}}}^{180}\right) - \left({u_{f_{21}}}^0 \ + \ {u_{f_{21}}}^{180}\right)\right] \quad (8)$$

and

$$R_{fund.\ harm.} = \left[{u_{f_1}}^0 - \frac{1}{2}\left({u_{f_1}}^0 \ + \ {u_{f_1}}^{180}\right)\right] \times \left[{u_{f_2}}^0 - \frac{1}{2}\left({u_{f_2}}^0 \ + \ {u_{f_2}}^{180}\right)\right]. \quad (9)$$

By considering the frequency spectrum of the signals in equations (8) and (9), and according to Figure 3, $R_{sideband}$ and $R_{fund.\ harm.}$ can be expressed based on the received amplitudes of harmonics and sidebands

$$\begin{aligned} R_{sideband} &= \left[\left(A_{f_1} + A_{2f_1} + A_{f_2} + A_{2f_2}\right) - 2A_{2f_1} - 2A_{2f_2}\right] \\ &\quad -\left[\left(A_{f_1} + A_{2f_1} + A_{f_2} + A_{2f_2} + A_s + A_d\ \right) - 2A_{2f_1} - 2A_{2f_2} - 2A_s - 2A_d\right] \\ &= \left(A_{f_1} + A_{f_2} - A_{2f_1} - A_{2f_2}\right) - \left(A_{f_1} + A_{f_2} - A_{2f_1} - A_{2f_2} - A_s - A_d\right) \\ &= A_s + A_d\ . \end{aligned} \quad (10)$$

and

$$\begin{aligned} R_{fund.\ harm.} &= \left[\left(A_{f_1} + A_{2f_1}\right) - A_{2f_1}\right] \times \left[\left(A_{f_2} + A_{2f_2}\right) - A_{2f_2}\right] \\ &= A_{f_1}A_{f_2}\ . \end{aligned} \quad (11)$$

Equation (10) can be then divided by (11), and the resulting ratio is equal to that of equation (6) in Section 2 (i.e. equal to $R_{\beta_s+\beta_d}$)

$$R_{\beta_s+\beta_d} = \frac{R_{sideband}}{R_{fund.\ harm.}} = \frac{A_s + A_d}{A_{f_1}A_{f_2}}\ . \quad (12)$$

4 Experimental Process

4.1 Aluminium and CFRP Test Samples

To assess the proposed approach, various samples made by two different materials, aluminium and CFRP, with multiples interfaces were manufactured. In the first case, aluminium disks with four holes (Figure 4a) were machined from a 6082-T6 aluminium round bar to different thicknesses (23, 19, 15, 11 and 7 mm). The maximum deviation in flatness was 0.03 mm and the surface finish equal to 0.1 µm. As illustrated in Figure 4, the disks were stacked in two separate orders and held under constant pressure using M4 bolts through the holes, that were all tightened to a maximum torque of 2.5 Nm. These two assemblies were used to simulate aluminium rods with contact interfaces at multiple depths. In this paper, the assemblies shown in Figure 4b and Figure 4c are referred as the aluminium test samples AL1 and AL2 respectively.

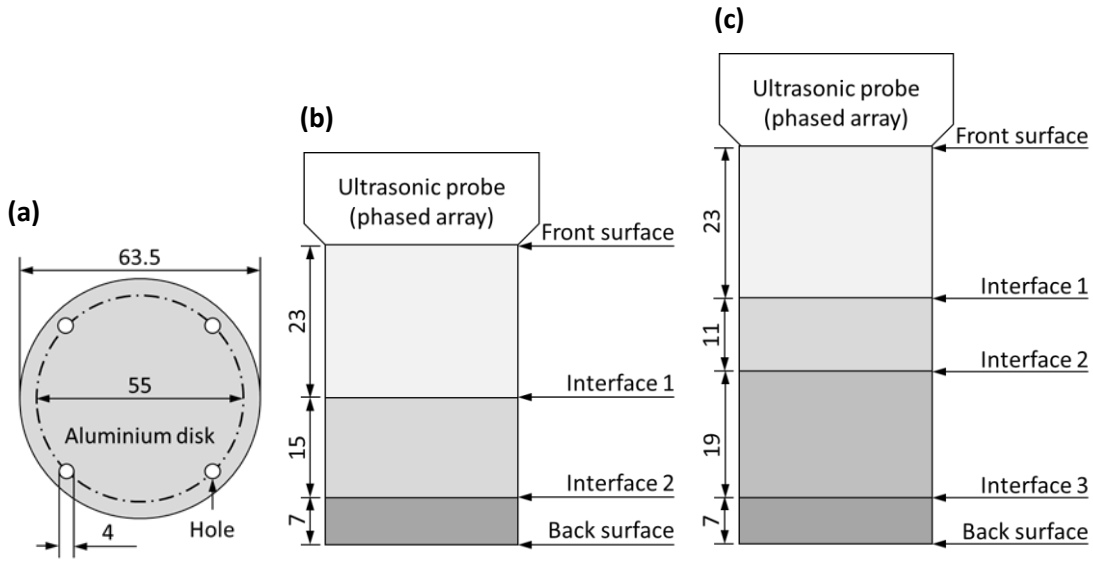

Figure 4: Size of aluminium disks (a) and their stacking sequence in test sample AL1 (b) and AL2 (c). Dimensions in mm. Not to scale.

Similarly, rectangular CFRP laminates (Figure 5a) of various thicknesses (13.5, 8.5 and 4.1 mm) were used for the assembly of two composite test samples. The laminates were made from unidirectional carbon-epoxy (Hexcel T800-M21) layers in quasi-isotropic orientation, but the exact number of layers and lay-up in each laminate was unknown. The flatness across the length and width of the laminates had a maximum deviation of 0.2 mm and 0.07 mm respectively, and the surface finish was measured as 0.15 µm. The stacking orders of the laminates in samples CFRP1 and CFRP2 are presented in Figure 5b and Figure 5c. The laminates forming each composite sample were also subject to fixed pressure, using one vice clamp on either end.

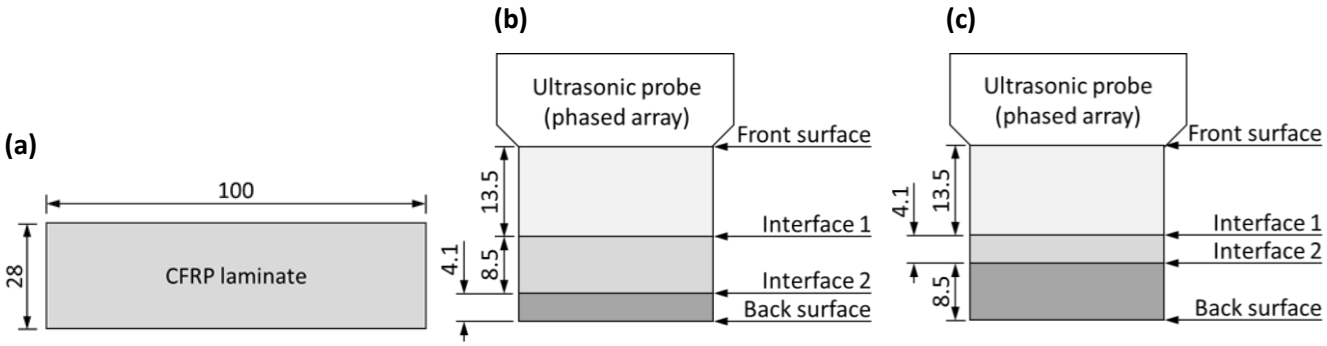

Figure 5: Size of composite laminates (a) and their stacking sequence in test sample CFRP1 (b) and CFRP2 (c). Dimensions in mm. Not to scale.

4.2 Phased Array Ultrasonic (Pulse-Echo) Tests

The following experimental activities were completed using a phased array system (from Diagnostic Sonar Ltd) equipped with a 5 MHz ultrasonic probe of 128 piezoelectric elements (pitch of 0.5 mm). In all cases, the probe was directly coupled to the top surface of the material using water-based gel and consistent coupling was maintained by resting a steel mass of 100 g on the probe. In addition, ultrasonic excitation was performed only at two frequencies, f_1 = 4.8 MHz and f_2 = 5.3 MHz, and the transmitted signals were sinusoidal waves of one cycle. These were close to the central frequency of the probe, meaning that the energy of the propagating waves was expected to be high. The tests on the aluminium samples were conducted using an input signal voltage of 20 V, whereas on the CFRP specimens the voltage was increased to 60V. This is because the waves travelling through the multi-layered composites with varying fibre orientation were expected to attenuate faster.

4.2.1 Speed of Sound Measurement

Prior to conducting acoustic inspection experiments, the average speed of ultrasound in the aluminium and CFRP samples was calculated through pulse-echo testing in accordance with the ASTM E494-15 standard. Specifically, the speed was measured on a single aluminium disk (23 mm thick), initially at 4.8 MHz and then at 5.3 MHz, suggesting an average value of 6420 m/s. In the same way, the mean velocity of ultrasound in the 13.5 mm thick CFRP laminate was estimated as 3040 m/s. These velocity values were used for the calculation of the expected positions of the contact interfaces in the time domain, as well as for the focusing of the transmitted signals.

4.2.2 Detection of Contact Interfaces in Test Samples

The aluminium and CFRP test specimens were then subject to ultrasonic pulse-echo tests for the detection of the contact interfaces in the form of amplitude peaks in the captured time domain. The phased array system was programmed to perform signal transmission in beams of 32 elements and in steps of one element (i.e. 97 beams in total). The waves reflected from the contact interfaces and the back surface of the samples were

recorded by the probe in the time domain and stored in the form of an image (B-scan). At this point it must be mentioned that around 10-15 beams on either end of the probe were located outside the top surface of the specimens, and hence, those beams were excluded from the analysis of data. The time signals associated with the remaining beams were summed up to obtain the combined ultrasonic signal of the material.

According to the method described in Section 3, four input signals were initially transmitted with a phase angle of 0° ($u_{f_1}{}^0$, $u_{f_2}{}^0$, $u_{f_{12}}{}^0$ and $u_{f_{21}}{}^0$) and then with a phase angle of 180° ($u_{f_1}{}^{180}$, $u_{f_2}{}^{180}$, $u_{f_{12}}{}^{180}$ and $u_{f_{21}}{}^{180}$), allowing the calculation of the nonlinear modulated response $R_{\beta_s+\beta_d}$ arising from the sum of β_s and β_d parameters (ref. equations (8)-(12)). For comparison, the linear ultrasonic response of the material was represented by the signal recorded under $u_{f_1}{}^0$ transmission (i.e. $R_{f_1} = u_{f_1}{}^0$).

5 Results and Discussion

The figures provided in this section show the signal processing steps followed for the plotting of the R_{f_1} and $R_{\beta_s+\beta_d}$ responses and their comparison. In all figures, the initial part of the signal was truncated to remove the near-field effect. In addition, the expected positions of the contact interfaces and the back surface were marked on the plot with vertical dashed lines. These positions were calculated based on the speed of sound in the material, as explained in Section 4.2.1. The original signals captured on AL1 sample in the cases of ${u_{f_1}}^0$, ${u_{f_2}}^0$, ${u_{f_{12}}}^0$ and ${u_{f_{21}}}^0$ transmission are illustrated in Figure 6. These are the exact inverse signals of those recorded under ${u_{f_1}}^{180}$, ${u_{f_2}}^{180}$, ${u_{f_{12}}}^{180}$ and ${u_{f_{21}}}^{180}$ transmission. By processing all the captured signals using the expressions from Section 3, the $R_{\beta_s+\beta_d}$ response was obtained. A normalised plot of $R_{\beta_s+\beta_d}$ against R_{f_1} ($= {u_{f_1}}^0$) is shown in Figure 7.

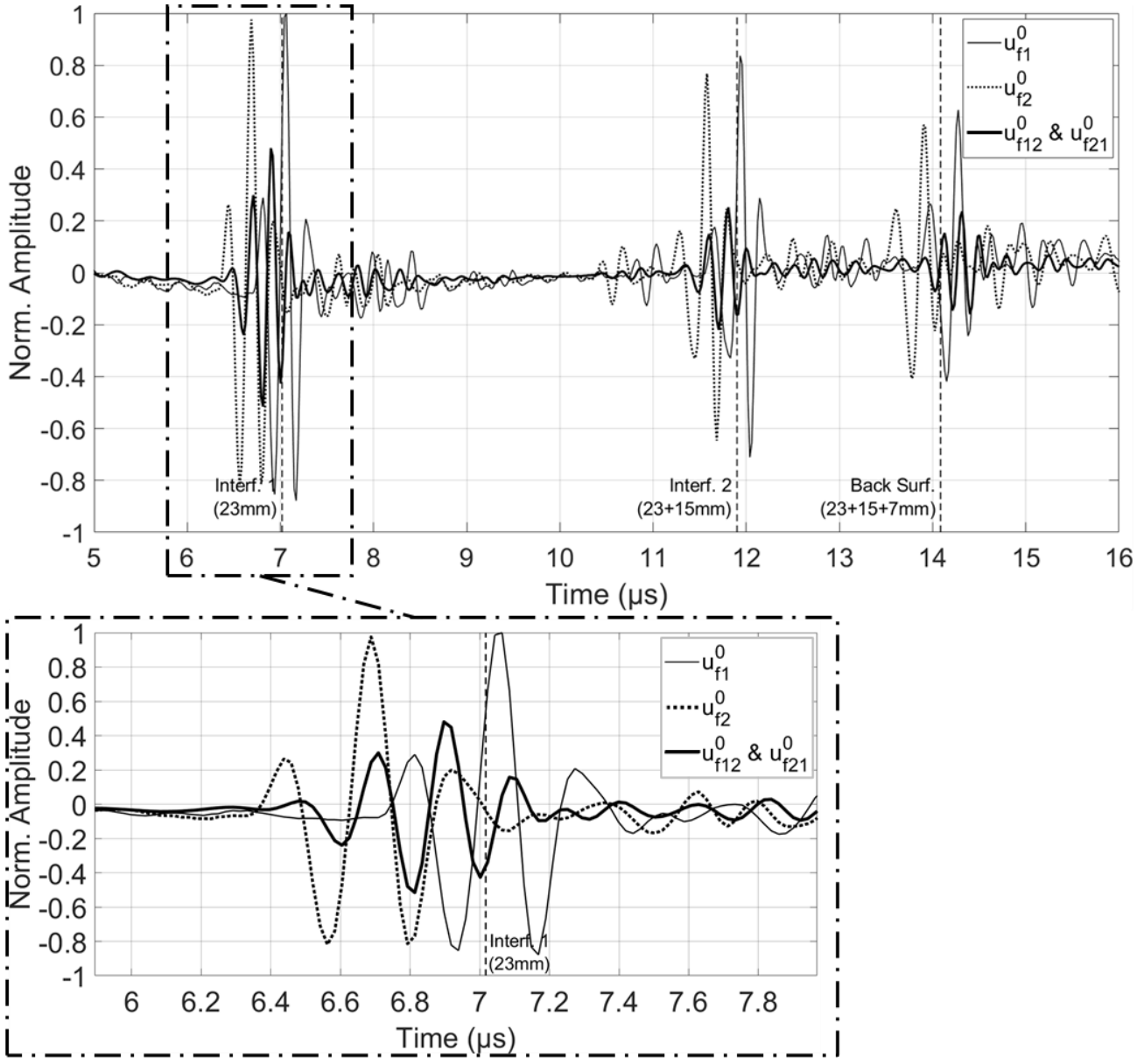

Figure 6: Normalised plot of the original signals captured on AL1 in the cases of $u_{f1}{}^0$, $u_{f2}{}^0$, $u_{f12}{}^0$ and $u_{f21}{}^0$ transmission.

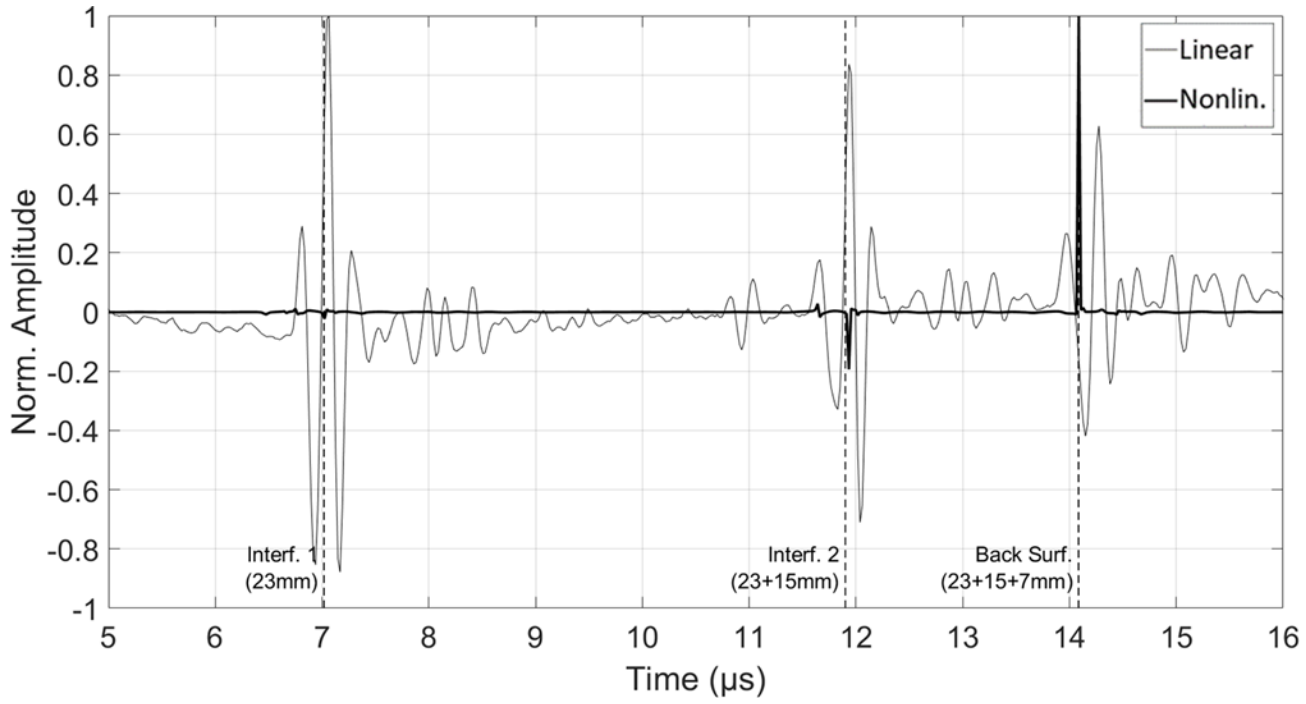

Figure 7: Normalised plot of the linear response against the nonlinear modulated response of sample AL1.

Then, in Figure 8a the absolute of $R_{\beta_s+\beta_d}$ was plotted against the Hilbert transform of R_{f_1} for easier visualisation. The same plot corresponding to the case of CFRP1 sample is shown in Figure 9a. According to Figure 8a and Figure 9a, both the R_{f_1} and $R_{\beta_s+\beta_d}$ responses included peaks close to the expected positions of the interfaces. By considering the attenuation of waves transmitted to deeper interfaces with almost the same size, shape and surface contact, then the amplitude of the peaks in the linear R_{f_1} response would be expected to have a decreasing trend as shown in Figure 8a. However, for a better surface contact at an interface, most of the incident wave could be transmitted through instead of being reflected to the source. As a result, the linear peaks corresponding to deeper interfaces (e.g. back wall) could have higher amplitudes as illustrated in Figure 9a. In the case of $R_{\beta_s+\beta_d}$, the amplitude of the peaks was expected to depend primarily on the level of nonlinearity at each contact interface (i.e. based on the characteristics of the interface). As can be seen in Figure 8a and Figure 9a, the peaks with the highest amplitude were those indicating the back surface. This could possibly be attributed to strong nonlinearities from the sample contact with the bolt heads or clamps used to hold under pressure the aluminium disks or composite laminates (ref. section 4.1). The reason is that the bolt/clamp material (steel/cast iron) is different from the sample material, meaning that the contact interface at the back wall is characterised by a steep change in acoustic impedance which results in strong reflection. Inversely, the interfaces within the sample separate two pieces of the same material (i.e. same acoustic impedance) and assuming that good contact is maintained then the reflection can be relatively weak.

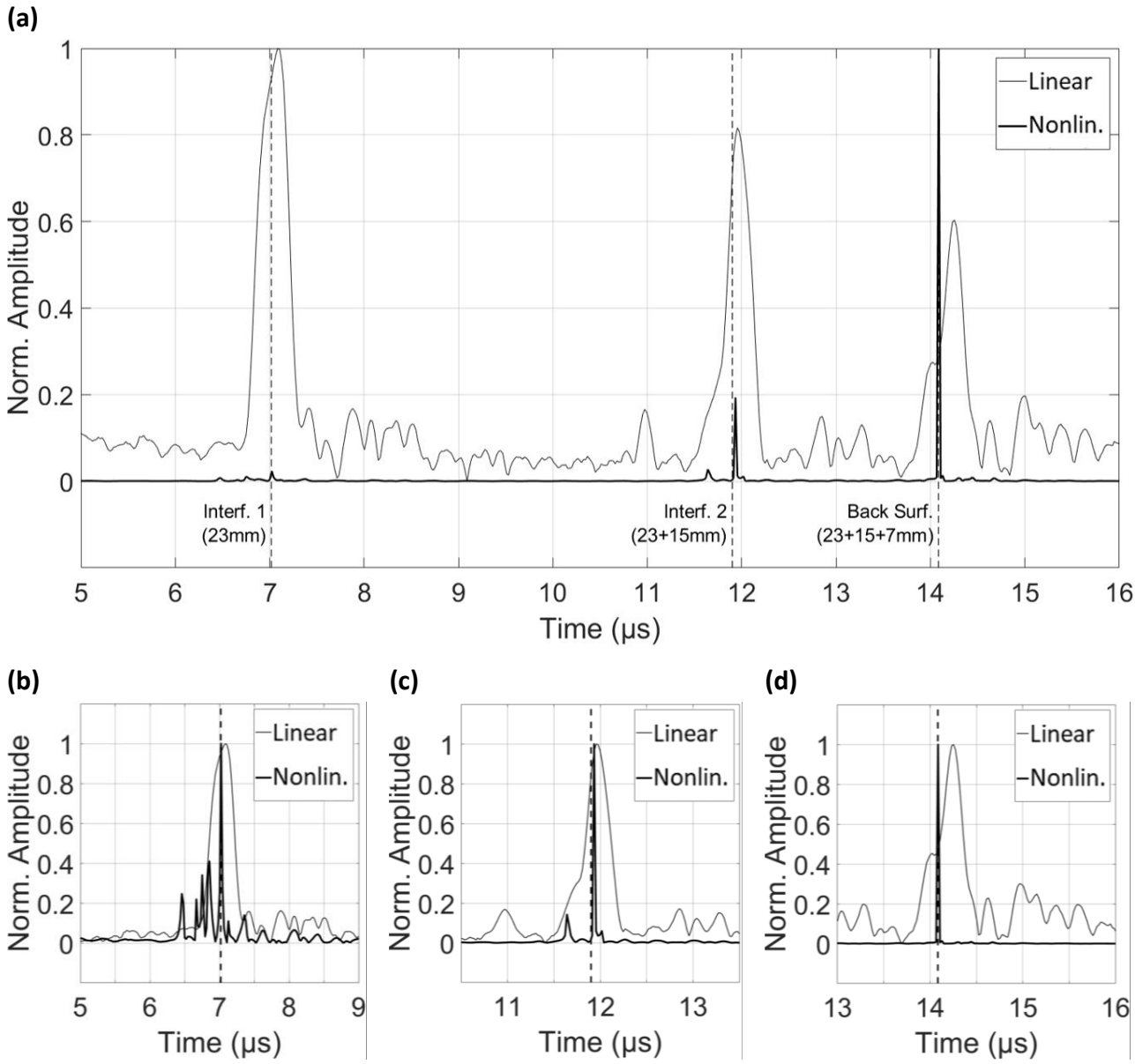

Figure 8: Hilbert transform of the linear response against the absolute nonlinear modulated response of sample AL1. Normalised plot showing the contact interfaces and back surface (a), and normalised plot around interface 1 (b), interface 2 (c) and back surface (d).

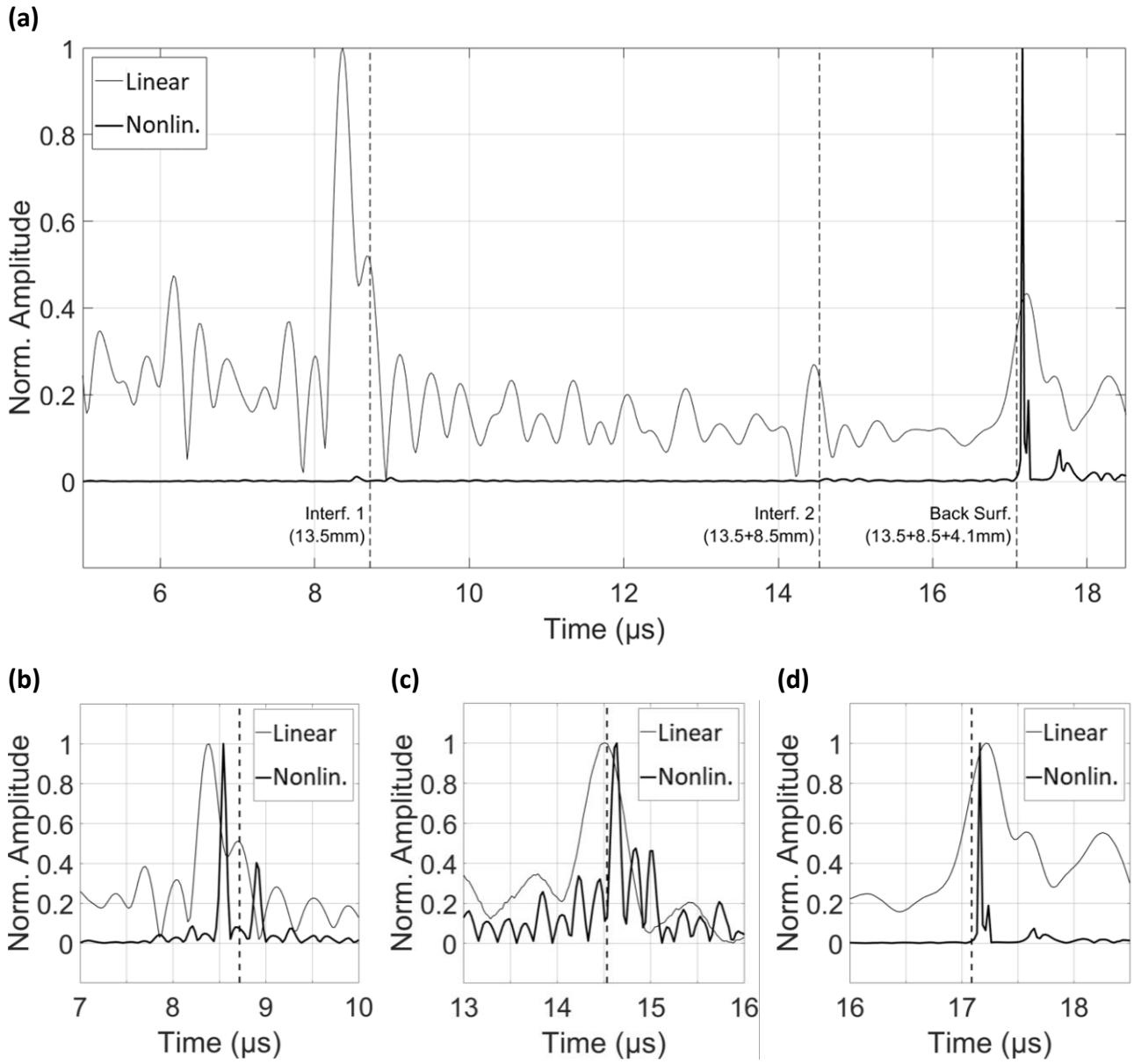

Figure 9: Hilbert transform of the linear response against absolute the nonlinear modulated response of sample CFRP1. Normalised plot showing the contact interfaces and back surface (a), and normalised plot around interface 1 (b), interface 2 (c) and back surface (d).

The linear and nonlinear modulated peaks at each interface could not be directly compared because the R_{f_1} and $R_{\beta_s+\beta_d}$ plots were individually normalised with respect to their maximum amplitude. Instead, the parts of the time domain around the locations of the interfaces were normalised separately, and plotted as illustrated in Figure 8b to Figure 8d for AL1, and Figure 9b to Figure 9d for CFRP1. The peaks in R_{f_1} and $R_{\beta_s+\beta_d}$ indicating the contact defects were compared based on three parameters. The first one was the magnitude of SNR which was calculated as

$$SNR = \frac{A_{peak}}{A_{noise}}, \tag{10}$$

where A_{peak} was the amplitude of every peak and A_{noise} was the amplitude of noise along the entire time domain. The value of A_{noise} was estimated as the mean amplitude of all values below 3 standard deviations.

The second parameter of comparison was the peak width at a 50% drop (i.e. 6 dB drop) from its maximum point. This is a common measure in literature, also known as the peak width at half-height (w_h), which can be used to indicate how localised (narrow) the peaks are. Also, the smaller the w_h value is the greater the possibility is to detect contact defects which may be located very close to the top or bottom surfaces of the material. This is obviously dependant on the strength of the near-field effect or the back wall reflection which is a limitation for all pulse-echo techniques. The last comparison was made based on the positioning error (ε_p) of the peaks in R_{f_1} and $R_{\beta_s+\beta_d}$ relative to the expected positions of the interfaces and back surface in the time domain (i.e. relative to the dashed lines in Figure 8 and Figure 9). Similar plots of linear ultrasonic and nonlinear modulated signal responses were obtained from the phased array experiments on the AL2 and CFRP2 samples. The results of SNR, w_h and ε_p from all four tests specimens were summarised in Table 1.

Table 1: SNR, w_h and ε_p of the peaks in R_{f1} and $R_{\beta s+\beta d}$ responses of aluminium and CFRP samples.

Sample	Response	Interface 1			Interface 2			Interface 3			Back Surface		
		SNR (−)	w_h (μs)	ε_p (μs)	SNR (−)	w_h (μs)	ε_p (μs)	SNR (−)	w_h (μs)	ε_p (μs)	SNR (−)	w_h (μs)	ε_p (μs)
AL1	R_{f_1}	14.31	0.37	0.07	11.68	0.29	0.07	–	–	–	8.63	0.27	0.02
	$R_{\beta_s+\beta_d}$	23.89	0.03	0.00	199.69	0.03	0.02	–	–	–	1030.93	0.02	0.00
AL2	R_{f_1}	12.67	0.29	0.01	6.18	0.29	0.05	9.96	0.26	0.23	4.04	0.40	0.31
	$R_{\beta_s+\beta_d}$	247.86	0.03	0.05	51.41	0.03	0.02	1020.41	0.03	0.05	188.88	0.09	0.02
CFRP1	R_{f_1}	5.56	0.51	0.32	1.48	0.48	0.02	–	–	–	2.41	0.5	0.13
	$R_{\beta_s+\beta_d}$	6.90	0.10	0.16	3.73	0.12	0.08	–	–	–	909.09	0.03	0.07
CFRP2	R_{f_1}	5.26	0.28	0.17	3.30	0.37	0.25	–	–	–	2.67	0.41	0.24
	$R_{\beta_s+\beta_d}$	7.60	0.09	0.14	8.47	0.09	0.05	–	–	–	1612.90	0.03	0.27

As can be seen, in all cases, the SNR values of the peaks in $R_{\beta_s+\beta_d}$ were significantly higher than those corresponding to the peaks in R_{f_1}. Regarding the aluminium samples, the difference in SNR was varying from a minimum of ~70% (interface 1 in AL1) up to a maximum of more than two orders of magnitude (back surface in AL1). The equivalent SNR variation in CFRP specimens was from ~25% (interface 2 in CFRP1) to nearly three orders of magnitude (back surface in CFRP2). The w_h measurements showed that in all samples the width of the peaks in the nonlinear modulated signal was much smaller than the peaks in the linear response. For the aluminium specimens, the difference in peak width was almost constant at around one order of magnitude. In the case of CFRP samples, the width of the nonlinear peaks at some interfaces (e.g. interfaces 1 and 2 in CFRP1) was smaller than that of the linear peaks by at least three times, whereas at other interfaces (e.g. back surface in CFRP1) by more than one order of magnitude. Regarding the positioning accuracy of the peaks, the nonlinear peaks offered smaller ε_p values than the linear peaks for the majority of the interfaces and back

surfaces (10 out of 13 cases). Also, in two cases the ε_p of nonlinear peaks was equal to zero. Most importantly though, the mean ε_p of the peaks in $R_{\beta_s+\beta_d}$ (0.07 μs) was around 45% smaller than the average ε_p of the peaks in R_{f_1} (0.16 μs). Finally, as a general observation, the majority of the peaks in both R_{f_1} and $R_{\beta_s+\beta_d}$ of the aluminium samples indicated higher SNR, smaller w_h and smaller ε_p values compared with those of CFRP specimens, which could be translated to lower accuracy in the detection of contact defects in CFRP samples. This could be true to some extent, considering that the CFRP laminates were not fully isotropic and their cut edges included broken fibres and cracked matrix. Hence, the propagation of nonlinear waves from the interfaces should not be as uniform as in the isotropic aluminium specimens. However, it must be noted that the SNR and w_h results from the aluminium samples should not be directly studied against those from the CFRP specimens, because of their differences in geometry, thickness and speed of sound.

6 Conclusions

This work introduced an alternative phased array (pulse-echo) method relying on the nonlinear ultrasonic modulation of elastic waves from dual-frequency excitation. The aim was to localise contact type defects at multiple interfaces in metallic and composite materials with higher sensitivity and accuracy, compared to the traditional linear phased array technique. The proposed method assessed the material nonlinearities based on the sum of β_s and β_d modulation parameters, that were obtained from effective signal processing involving the use of pulse inversion technique in some steps. Phased array experiments were conducted on two circular aluminium samples and two rectangular CFRP specimens containing contact interfaces at different depths through the thickness. The received linear ultrasonic and nonlinear modulated responses (R_{f_1} and $R_{\beta_s+\beta_d}$) were plotted in the time domain, and as explained in the previous section, their peaks indicating the positions of the contact interfaces and the back surfaces were compared based on the values of SNR, w_h and ε_p. The results revealed that for all four test samples, the SNR associated with the peaks in $R_{\beta_s+\beta_d}$ signal was higher than the SNR of the peaks in R_{f_1} response, with a maximum difference of around three orders of magnitude. Similarly, the results of w_h measurements suggested that, in all cases, the nonlinear peaks were narrower compared with the linear peaks, and the largest difference in width was more than one order of magnitude. Lastly, the mean value of ε_p corresponding to the peaks in $R_{\beta_s+\beta_d}$ was on around 45% smaller than that of the peaks in R_{f_1}. In conclusion, this work proved that the presented nonlinear phased array method enabled the identification of multiple contact flaws in the test specimens with significantly higher sensitivity and localisation accuracy relative to the conventional linear phased array method. This technique could potentially be implemented in the design of future phased array systems for enhanced performance in pulse-echo inspection of metallic and composite structures. Future work should assess the performance of the technique against that of linear ultrasonic inspection in more realistic scenarios such as the case of samples containing significantly smaller contact defects (e.g. fatigue cracks) that are not necessarily located exactly one on top of the other or covering the entire plane of the material. Another topic for future study could be the focusing of

the phased array signals on multiple points throughout the specimen instead of only the bottom surface, to examine how this affects the sensitivity of the method, even though this will more time consuming.

References

1. Donskoy, D., Sutin, A., & Ekimov, A. (2001). Nonlinear acoustic interaction on contact interfaces and its use for nondestructive testing. *NDT & E International*, 34(4), 231-238.
2. Kim, J. Y., & Lee, J. S. (2007). A micromechanical model for nonlinear acoustic properties of interfaces between solids. *Journal of Applied Physics*, 101(4), 043501.
3. Bastianini, F., Di Tommaso, A., & Pascale, G. (2001). Ultrasonic non-destructive assessment of bonding defects in composite structural strengthenings. *Composite Structures*, 53(4), 463-467.
4. Benammar, A., Drai, R., & Guessoum, A. (2008). Detection of delamination defects in CFRP materials using ultrasonic signal processing. *Ultrasonics*, 48(8), 731-738.
5. Kato, Y., Tanaka, H., & Sugiura, T. (2015). Detection of low-frequency components in ultrasonic waves transmitted through contact solids. In *2015 IEEE International Ultrasonics Symposium* (Vol. 1, p. 1-4). IEEE.
6. Yeh, F. W. T., Lukomski, T., Haag, J., Clarke, T., Stepinski, T., & Strohaecker, T. R. (2018). An alternative ultrasonic Time-of-Flight Diffraction (TOFD) method. *NDT & E International*, 100(1), 74-83.
7. Drinkwater, B. W., & Wilcox, P. D. (2006). Ultrasonic arrays for non-destructive evaluation: A review. *NDT & E International*, 39(7), 525-541.
8. Bai, Z., Chen, S., Xiao, Q., Jia, L., Zhao, Y., & Zeng, Z. (2018). Compressive sensing of phased array ultrasonic signal in defect detection: Simulation study and experimental verification. *Structural Health Monitoring*, 17(3), 434-449.
9. Caminero, M. A., Garcia-Moreno, I., Rodriguez, G. P., & Chacon, J. M. (2019). Internal damage evaluation of composite structures using phased array ultrasonic technique: Impact damage assessment in CFRP and 3D printed reinforced composites. *Composites Part B: Engineering*, 165(1), 131-142.
10. Safari, A., Zhang, J., Velichko, A., & Drinkwater, B. W. (2018). Assessment methodology for defect characterisation using ultrasonic arrays. *NDT & E International*, 94(1), 126-136.
11. Taheri, H., & Hassen, A. A. (2019). Nondestructive ultrasonic inspection of composite materials: a comparative advantage of phased array ultrasonic. *Applied Sciences*, 9(8), 1628.
12. Zhang, J., Drinkwater, B. W., & Wilcox, P. D. (2010). The use of ultrasonic arrays to characterize crack-like defects. *Journal of Nondestructive Evaluation*, 29(4), 222-232.
13. Tant, K. M., Mulholland, A. J., & Gachagan, A. (2015). A model-based approach to crack sizing with ultrasonic arrays. *IEEE transactions on ultrasonics, ferroelectrics, and frequency control*, 62(5), 915-926.
14. Van Pamel, A., Huthwaite, P., Brett, C. R., & Lowe, M. J. (2016). Numerical simulations of ultrasonic array imaging of highly scattering materials. *NDT & E International*, 81(1), 9-19.
15. Jiao, J., Ma, T., Hou, S., Wu, B., & He, C. (2018). A Pulse Compression Technique for Improving the Temporal Resolution of Ultrasonic Testing. *Journal of Testing and Evaluation*, 46(3), 1238-1249.
16. Mohammadkhani, R., Zanotti Fragonara, L., Padiyar M, J., Petrunin, I., Raposo, J., Tsourdos, A., & Gray, I. (2020). Improving Depth Resolution of Ultrasonic Phased Array Imaging to Inspect Aerospace Composite Structures. *Sensors*, 20(2), 559.
17. Zhang, J., Drinkwater, B. W., Wilcox, P. D., & Hunter, A. J. (2010). Defect detection using ultrasonic arrays: The multi-mode total focusing method. *NDT & E International*, 43(2), 123-133.

18. Abdessalem, B., Ahmed, K., & Redouane, D. (2017). Signal Quality Improvement Using a New TMSSE Algorithm: Application in Delamination Detection in Composite Materials. *Journal of Nondestructive Evaluation*, 36(1), 16.

19. Ohara, Y., Shintaku, Y., Horinouchi, S., Ikeuchi, M., & Yamanaka, K. (2012). Enhancement of selectivity in nonlinear ultrasonic imaging of closed cracks using amplitude difference phased array. *Japanese Journal of Applied Physics*, 51(7S), 07GB18.

20. Kawashima, K., Murase, M., Yamada, R., Matsushima, M., Uematsu, M., & Fujita, F. (2006). Nonlinear ultrasonic imaging of imperfectly bonded interfaces. *Ultrasonics*, 44(1), 1329-1333.

21. Kundu, T. (2019). *Nonlinear ultrasonic and vibro-acoustical techniques for nondestructive evaluation*. Cham: Springer.

22. Buck, O., Morris, W. L., & Richardson, J. M. (1978). Acoustic harmonic generation at unbonded interfaces and fatigue cracks. *Applied Physics Letters*, 33(5), 371-373.

23. Soleimanpour, R., Ng, C. T., & Wang, C. H. (2017). Higher harmonic generation of guided waves at delaminations in laminated composite beams. *Structural Health Monitoring*, 16(4), 400-417.

24. Sasaki, R., Ogata, T., Ohara, Y., Mihara, T., & Yamanaka, K. (2005). Simulation and analysis of subharmonics and tail effect for ultrasonic nondestructive evaluation of closed cracks. *Japanese Journal of Applied Physics*, 44(6S), 4389.

25. Seo, H., Pyun, D. K., & Jhang, K. Y. (2019). Synthetic aperture imaging of contact acoustic nonlinearity to visualize the closing interfaces using tone-burst ultrasonic waves. *Mechanical Systems and Signal Processing*, 125(1), 257-274.

26. Ohara, Y., Mihara, T., Sasaki, R., Ogata, T., Yamamoto, S., Kishimoto, Y., & Yamanaka, K. (2007). Imaging of closed cracks using nonlinear response of elastic waves at subharmonic frequency. *Applied Physics Letters*, 90(1), 011902.

27. Sugawara, A., Jinno, K., Ohara, Y., & Yamanaka, K. (2015). Closed-crack imaging and scattering behavior analysis using confocal subharmonic phased array. *Japanese Journal of Applied Physics*, 54(7S1), 07HC08.

28. Ohara, Y., Mihara, T., & Yamanaka, K. (2019). Subharmonic Phased Array for Crack Evaluation (SPACE). In *Nonlinear Ultrasonic and Vibro-Acoustical Techniques for Nondestructive Evaluation* (Vol. 1, p. 419-469). Cham: Springer.

29. Park, C. S., Kim, J. W., Cho, S., & Seo, D. C. (2016). A high resolution approach for nonlinear sub-harmonic imaging. *NDT & E International*, 79(1), 114-122.

30. Potter, J. N., Croxford, A. J., & Wilcox, P. D. (2014). Nonlinear ultrasonic phased array imaging. *Physical Review Letters*, 113(14), 144301.

31. Cheng, J., Potter, J. N., & Drinkwater, B. W. (2018). The parallel-sequential field subtraction technique for coherent nonlinear ultrasonic imaging. *Smart Materials and Structures*, 27(6), 065002.

32. Fierro, G. P. M., & Meo, M. (2018). IWSHM 2017: Structural health monitoring of the loosening in a multi-bolt structure using linear and modulated nonlinear ultrasound acoustic moments approach. *Structural Health Monitoring*, 17(6), 1349-1364.

33. Van Den Abeele, K. A., Johnson, P. A., & Sutin, A. (2000). Nonlinear elastic wave spectroscopy (NEWS) techniques to discern material damage, part I: nonlinear wave modulation spectroscopy (NWMS). *Journal of Research in Nondestructive Evaluation*, 12(1), 17-30.

34. Chen, B. Y., Soh, S. K., Lee, H. P., Tay, T. E., & Tan, V. B. (2016). A vibro-acoustic modulation method for the detection of delamination and kissing bond in composites. *Journal of Composite Materials*, 50(22), 3089-3104.

35. Zagrai, A., Donskoy, D., & Lottiaux, J. L. (2004). N-Scan: New Vibro-Modulation System for Crack Detection, Monitoring and Characterization. In *AIP Conference Proceedings* (Vol. 700, No. 1, p. 1414-1421). AIP Publishing.

36. Zhang, Z., Xu, H., Liao, Y., Su, Z., & Xiao, Y. (2017). Vibro-acoustic modulation (VAM)-inspired structural integrity monitoring and its applications to bolted composite joints. Composite Structures, 176(1), 505-515.

37. Dunn, M. (2018). *Nonlinear vibro-ultrasonics for detection of damage and weak bonds in composites*. Thesis (Doctoral), The University of Queensland.

38. Sohn, H., Liu, P., Lim, H. J., & Park, B. (2019). Noncontact Nonlinear Ultrasonic Wave Modulation for Fatigue Crack and Delamination Detection. In *Nonlinear Ultrasonic and Vibro-Acoustical Techniques for Nondestructive Evaluation* (Vol. 1, p. 661-697). Cham: Springer.

39. Haupert, S., Renaud, G., & Schumm, A. (2017). Ultrasonic imaging of nonlinear scatterers buried in a medium. *NDT & E International*, 87(1), 1-6.

40. Haupert, S., Ohara, Y., Carcreff, E., & Renaud, G. (2019). Fundamental wave amplitude difference imaging for detection and characterization of embedded cracks. *Ultrasonics*, 96(1), 132-139.

41. Alston, J., Croxford, A., Potter, J., & Blanloeuil, P. (2018). Nonlinear non-collinear ultrasonic detection and characterisation of kissing bonds. *NDT & E International*, 99(1), 105-116.

42. Fierro, G. P. M., & Meo, M. (2019). Nonlinear phased array imaging of flaws a modulation technique. In *Nondestructive Characterization and Monitoring of Advanced Materials, Aerospace, Civil Infrastructure, and Transportation XIII* (Vol. 10971, p. 1097116). International Society for Optics and Photonics.

43. Ohara, Y., Kawashima, K., Yamada, R., & Horio, H. (2004). Evaluation of amorphous diffusion bonding by nonlinear ultrasonic method. In *AIP Conference Proceedings* (Vol. 700, p. 944-951). AIP Publishing.

44. Xie, F., Guo, Z., & Zhang, J. (2014). Strategies for reliable second harmonic of nonlinear acoustic wave through cement-based materials. *Nondestructive Testing and Evaluation*, 29(3), 183-194.

45. Richardson, J. M. (1979). Harmonic generation at an unbonded interface - I. Planar interface between semi-infinite elastic media. *International Journal of Engineering Science*, 17(1), 73-85.

46. Biwa, S., Nakajima, S., & Ohno, N. (2004). On the acoustic nonlinearity of solid-solid contact with pressure-dependent interface stiffness. *Journal of Applied Mechanics*, 71(4), 508-515.

47. Guo, X., Zhang, D., & Wu, J. (2010). Quantitative evaluation of contact stiffness between pressed solid surfaces using dual-frequency ultrasound. *Journal of Applied Physics*, 108(3), 034902.

48. Kim, J. Y., Jacobs, L. J., Qu, J., & Littles, J. W. (2006). Experimental characterization of fatigue damage in a nickel-base superalloy using nonlinear ultrasonic waves. *The Journal of the Acoustical Society of America*, 120(3), 1266-1273.

49. Blanloeuil, P., Meziane, A., & Bacon, C. (2014). Numerical study of nonlinear interaction between a crack and elastic waves under an oblique incidence. *Wave Motion*, 51(3), 425-437.

50. Malfense Fierro, G. P., Ciampa, F., & Meo, M. (2020). Phase symmetry analysis for nonlinear ultrasonic modulated signals. *Structural Control and Health Monitoring*, 27(5), 2516.